Key Points:
- We assess the capability of the PFSS+SCS models adopted by EUHFORIA in reconstructing CH areas
- The heights of the source surface and the inner boundary of the SCS model impact the results
- Lower values for these two heights improved the results

Reconstructing Coronal Hole Areas With EUHFORIA and Adapted WSA Model: Optimizing the Model Parameters

E. Asvestari[1,2] ID, S. G. Heinemann[1] ID, M. Temmer[1] ID, J. Pomoell[2], E. Kilpua[2] ID, J. Magdalenic[3], and S. Poedts[4] ID

[1]Institute of Physics, University of Graz, Graz, Austria, [2]Department of Physics, University of Helsinki, Helsinki, Finland, [3]Solar-Terrestrial Centre of Excellence - SIDC, Royal Observatory of Belgium, Brussels, Belgium, [4]Centre for mathematical Plasma Astrophysics (CmPA), KU Leuven, Leuven, Belgium

Abstract The adopted Wang-Sheeley-Arge (WSA) model embedded in EUHFORIA (EUropean Heliospheric FORecasting Information Asset) is compared to EUV observations. According to the standard paradigm, coronal holes are sources of open flux; thus, we use remote sensing EUV observations and CATCH (Collection of Analysis Tools for Coronal Holes) to extract CH areas and compare them to the open flux areas modeled by EUHFORIA. From the adopted WSA model we employ only the Potential Field Source Surface (PFSS) model for the inner corona and the Schatten Current Sheet (SCS) model for the outer (PFSS+SCS). The height, R_{ss}, of the outer boundary of the PFSS, known as the source surface, and the height, R_i, of the inner boundary of the SCS are important parameters affecting the modeled CH areas. We investigate the impact the two model parameters can have in the modeled results. We vary R_{ss} within the interval $[1.4, 3.2]R_\odot$ with a step of $0.1R_\odot$, and R_i within the interval $[1.3, 2.8]R_\odot$ with the same step, and the condition that $R_i < R_{ss}$. This way we have a set of 184 initial parameters to the model, and we assess the model results for all these possible height pairs. We conclude that the default heights used so far fail in modeling accurately CH areas and lower heights need to be considered.

1. Introduction

The ambient solar wind (SW) and the frozen-in open magnetic field sculpt the medium through which coronal mass ejections (CMEs) and solar energetic particles (SEPs) propagate. Consequently, modeling the SW with high accuracy is a significant component toward more reliable space weather forecasts. Fast SW and open magnetic field are primarily associated with coronal holes (CHs; Levine et al., 1977; Schwenn, 2006a, 2006b; Wang et al., 1996), which in X-ray and extreme-ultraviolet (EUV) imaging observations can be identified as dark structures in the solar corona. Their dark appearance at these wavelengths is a result of having significantly lower density and temperature compared to their surroundings. Although a plethora of both empirical and intricate magnetohydrodynamic (MHD) models exists, due to its simplicity and comparability to computationally expensive MHD ones (MacNeice et al., 2018; Riley et al., 2006), the semiempirical Wang-Sheeley-Arge (WSA) model (Arge & Pizzo, 2000) is the model most commonly employed for estimating the SW flow close to the Sun. Its magnetic field model comprises the Potential Field Source Surface (PFSS; Altschuler & Newkirk, 1969; Schatten et al., 1969) and the Schatten Current Sheet (SCS; Schatten, 1971) models to extract the SW speed and the magnetic field in the corona and then by using a 1-D kinematic scheme attempts to predict the SW speed at Earth.

Being an empirical model, the WSA consists of a parametrization including several free parameters, which throughout the decades have been fitted and refitted to conform in situ observations of the SW plasma at 1 AU. One such parameter is the height of the outer boundary of the PFSS model, known as the source surface. In the traditional WSA model it serves as the inner boundary to the SCS model (Arge & Pizzo, 2000; Wang & Sheeley, 1990, 1992). The source surface and its distance from the Sun, R_{ss}, divide the corona into two zones; the inner and outer. Field lines piercing through the source surface are considered as open, while those forming closed loops below it are identified as belonging to closed magnetic structures. Open field lines are stretched out and away in the heliosphere by the SW forming the interplanetary magnetic field (IMF) (e.g., Wang & Sheeley, 2003). The PFSS does not account for dynamic effects that are especially important at the top of streamers (e.g., the high closed loops; Arge et al., 2002). Due to the association of open field to CHs, the areas on the source surface that are defined by concentration of open field lines map down to (one or
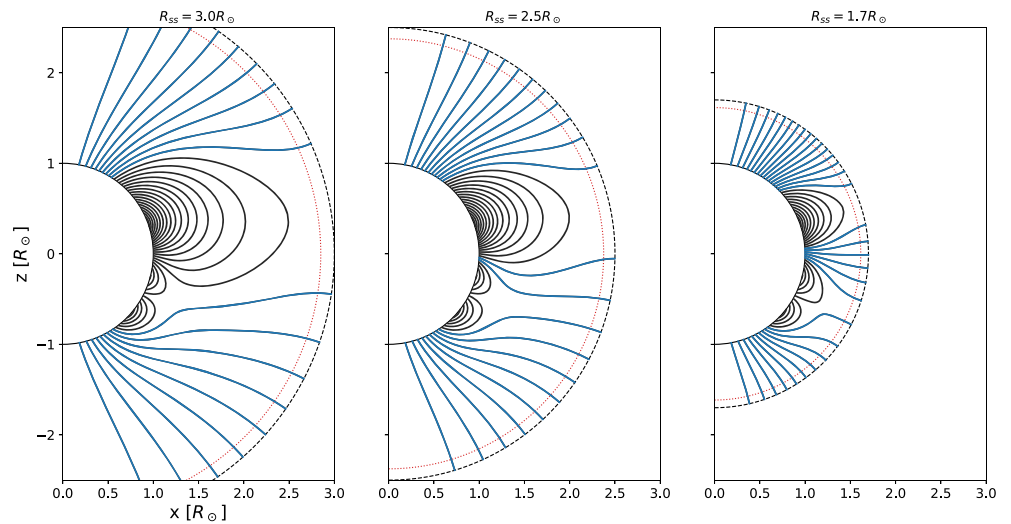
Figure 1. Schematic representation of the impact of the source surface height in the open and closed field line assignment. The coronal domain is divided into the inner and outer corona by the source surface (dashed black line), which acts as the outer boundary of the PFSS model. The red dotted line represent the inner boundary of the SCS model, which approximates the magnetic field in the outer corona. The lower the two boundaries are placed, the more field lines are considered as open. Resulting to bigger open field areas.

more) CHs. The location/height of R_{ss} determines strongly the total area of open field regions rooted in the low corona. Lowering R_{ss} will result in more field lines being open, and subsequently in larger areas of CHs. On the contrary, increasing it will reduce the number of open field lines and thus shrinking CH areas. This is visualized in Figure 1, where lowering the source surface expands the areas of open flux. Qualitatively, some field lines that were forming closed loops for the case of a source surface at height 3.0 solar radii are crossing through the source surface placed at height 2.5 solar radii and therefore are not considered closed anymore. Decreasing the source surface height even lower to 1.7 solar radii will result in increasing the number of closed loops that are becoming open and, therefore, in further growing of the open flux areas.

Since fast SW and open magnetic field are related to CHs, for the WSA model to successfully reconstruct the in situ measured SW properties and the open magnetic flux, it should model the size and geometry of CHs as accurately as possible. The dependence of the latter on the source surface height makes the choice of R_{ss} a definitive element in the model's success.

Selecting the optimal source surface height has been a long-standing debate. Earlier studies (e.g., Altschuler & Newkirk, 1969) indicated that the source surface is best placed at $2.5R_\odot$ ($R_\odot = 1$ solar radius). This value has been adopted by many as the canonical height; however, a range of values from $1.6R_\odot$ to $3.25R_\odot$ have been used (e.g., Arden et al., 2014). Criteria for the choice of these values have been (i) the sector structure of the Heliospheric Current Sheet (HCS; Hoeksema et al., 1982, 1983; Hoeksema & Scherrer, 1986), (ii) in situ and remote observations of the HCS by Ulysses (Phillips et al., 1994; Wang & Sheeley, 1995) and during total solar eclipses (Schatten et al., 1969), (iii) the IMF polarity (Hoeksema et al., 1983), (iv) the CH boundaries, (v) the IMF strength (e.g., Lee et al., 2011), and (vi) other coronal signatures that can be sources of open field (Levine, 1982). While plenty of studies were restricted to and/or concluded the use of a singular value for R_{ss} (Altschuler & Newkirk, 1969; Arge & Pizzo, 2000; Hoeksema et al., 1983; Linker et al., 2017; Luhmann et al., 2002, 2009, 2013; McGregor et al., 2008; Riley et al., 2006, 2015; Wang, 2009), others have been suggesting a solar cycle-dependent source surface height (e.g., Arden et al., 2014; Lee et al., 2011; Levine, 1982), a concept known as the "breathing" source surface (termed by Arden et al., 2014). In addition to that concept, the idea of a nonspherically shaped source surface has also been proposed (e.g., Levine et al., 1982; Riley et al., 2006; Schulz et al., 1978; Schulz, 1997, 2008).

Aiming to eliminate a known discontinuity in the WSA model, namely, kinks in the field lines occurring at the transition from the low-coronal PFSS to the high-coronal SCS domain, caused by the PFSS solution forcing the magnetic field to be radial at the source surface, McGregor et al. (2008) repositioned the inner boundary of the SCS model at a radius R_i lower than the source surface ($R_i < R_{ss}$). This concept is illustrated

in Figure 1, where the red dotted curve encircling the Sun represents the new inner boundary of the SCS model and the gray dashed curve is the source surface placed at height R_{ss}. As discussed in McGregor et al. (2008), these field line kinks are produced by a discontinuity in the latitudinal and longitudinal components of the field at the source surface. This implies the presence of surface current flows there. McGregor et al. (2008) introduced the lower SCS model inner boundary to minimize the currents flowing, and they demonstrated that not only they achieved that to some extent but, in addition, these changes improved SW speed predictions at Earth. Consequently, placing the inner boundary of the SCS modeling domain lower than the source surface boundary lead to an overall advancement of the WSA model. In establishing the optimal pair of $[R_i, R_{ss}]$ heights for their new adaptation of the WSA model, McGregor et al. (2008) aimed for conservation of the absolute total magnetic flux between the one from the original WSA model and that from their updated version. The purpose of that was to facilitate the comparison between the two models, original and improved WSA. The pair they deduced in their study is $[2.3, 2.6]R_{\odot}$ for R_i and R_{ss}, respectively.

EUHFORIA (EUropean Heliospheric FORecasting Information Asset) is a novel heliospheric wind and CME evolution model (Pomoell & Poedts, 2018) consisting of two main building blocks, the coronal model and the heliospheric full MHD model. The coronal model aims to reconstruct the SW plasma and the open flux conditions in the upper corona at $21.5R_{\odot}$, which serve as boundary conditions to the heliospheric model. It implements for that purpose the WSA model, with the McGregor et al. (2008) improvements (for more details read Pomoell & Poedts, 2018). The default $[R_i, R_{ss}]$ pair of heights is the one proposed by McGregor et al. (2008). In a comprehensive study of modeling the background SW with EUHFORIA using the adopted WSA model and default heights (Hinterreiter et al., 2019), it became evident that the capability of the model to predict a high-speed stream at Earth is often quite low, with predicted high-speed streams either shifted in time, having lower than expected amplitude in the SW speed profiles or being overall absent. Similar results have been reported in other physics-based reconstructions of the ambient SW (Gressl et al., 2014; Jian et al., 2011; Lee et al., 2009; Owens et al., 2008). The novelty of our study is the assessment of the PFSS+SCS capability to reconstruct CH areas with accuracy, knowing the relation between CHS and high-speed streams.

In the model the source surface and the SCS inner boundary positions are adjustable parameters. Considering the freedom in the choice of the source surface height, already brought forward by other studies discussed above, we focused first in qualitatively assessing the default values of $[R_i, R_{ss}]$ and subsequently in investigating the possibility of other height choices. To do that, we selected a sample of 15 CHs located around the central meridian of the solar disk as viewed from Earth, but at different latitudes (see section 2.2). Using CATCH (Collection of Analysis Tools for Coronal Holes; Heinemann et al., 2019), we extracted the boundaries of these CHs based on their appearance in EUV filtergrams at 193 Å (section 2.3). We reconstructed their areas with EUHFORIA, by varying the paired values for the heights of the source surface and the inner boundary of the SCS model, in order to find optimal values that produce a better match between modeled and observed CH areas (section 2.4). A quantitative analysis of the results was performed by defining two parameters, the coverage (*cov*) and the connected pixels area of open flux associated to the CH, of which we consider the percentage that lies within the EUV defined CH boundaries (CA_{in}). By coverage, in the context of this paper, it is meant the percentage of the CH area observed in EUV that is successfully modeled as open field area. And by connected pixels we consider the open field pixels that lie both inside and outside the EUV-defined CH boundary, and which form a continuous open field region that has the same polarity as the CH in study. Both parameters are analytically described in section 3.

From this study we conclude that the PFSS+SCS part of the adopted WSA model for the default heights of $[2.3, 2.6]R_{\odot}$ does not properly reconstruct CH areas. Lowering the heights $[R_i, R_{ss}]$ improved the model results; that is, open field lines are rooted to areas in the lower corona that better represented the CHs observed in EUV images. However, it also led in the presence of open field lines that mapped down to the corona at areas lying outside the CH boundaries defined via observations. This is an undesirable modeling effect, and we attempted to identify optimal height pair candidates by selecting those who lead to a modeling result that has improved CH area reconstruction without expanding the CH area beyond the expected boundaries.
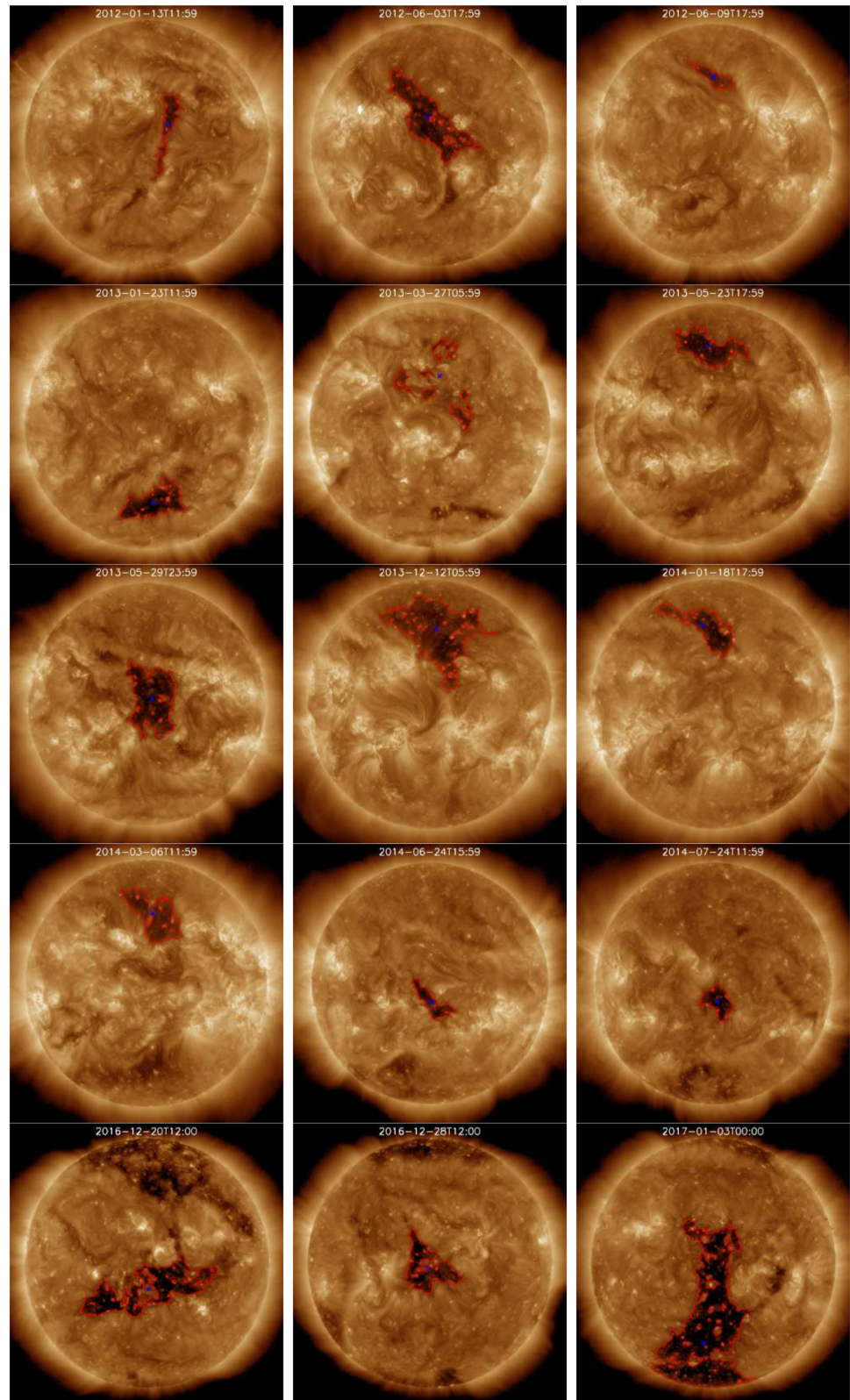
Figure 2. EUV filtergrams at 193 Å depicting the selected CHs in chronological order. The red curves mapping out the boundaries of the CHs are the optimal ones defined using CATCH.

2. Data and Methodologies

2.1. Observational Data

To compute the SW and magnetic field in the corona, the WSA model requires a magnetogram as input. The model performs a global corona simulation and outputs open-closed field regions for the entire solar surface. However, we focus our analysis to the results for the front side of the Sun, from Earth's perspective, where the selected CHs are located. We also do not analyze results toward the limb, with one exception, that of the CH on 3 January 2017, which is linked to a polar CH. Even though a variety of magnetograms are available, we used exclusively magnetograms provided by the Global Oscillation Network Group (GONG) and developed with the Air Force Data Assimilative Photospheric flux Transport (ADAPT) model. The aim was a coherent output and to avoid any effects on the modeled results due to quantitative differences among magnetograms (Riley et al., 2014), as a result of being obtained at different observatories, with different instruments, and constructed following various distinct techniques. These are synchronic magnetograms, meaning they are developed such as to resemble with high accuracy the magnetic field of the solar surface on a particular time. A detailed description of the ADAPT model can be found in Arge et al. (2010) and Hickmann et al. (2015), while the GONG-ADAPT database from which magnetograms were acquired is available online (ftp://gong. nso.edu/adapt/maps/gong/).

For extracting the CH boundaries we used EUV observations during 2012–2017 from the Atmospheric Imaging Assembly (AIA; Lemen et al., 2012) on board the Solar Dynamic Observatory (SDO; Pesnell et al., 2012). For this study we utilized the full disk coronal images (1,024 × 1,024) at a wavelength of 193 Å, which are made available by the Joint Science Operation Center (JSOC). Although it is argued that CHs appear differently when observed at different wavelengths, that is, varying boundaries, the 193 Å filter is most commonly used. The response function of this filter is most sensitive in the temperature range of quiet sun and CH regions resulting in a high contrast. Using these data, we extract the CH area and its boundary in a manner described in section 2.3.

2.2. Selected CHs

The 15 selected CHs are shown in chronological order in Figure 2. As mentioned earlier, all CHs have longitudinal position of center of mass (CoM) located along or within 10° of the central meridian of the Sun. The CoM longitude is calculated from the central meridian viewed from Earth in Stonyhurst coordinate system, where the central meridian has longitude equal to 0°. Although negative values of the CoM longitude are possible, the CH sample we worked with, nondeliberately, includes CHs with positive CoM longitude. The latitudinal position of their CoM varies from low to high latitudes. Limiting the sample to CHs located only along the central meridional zone provides the opportunity to focus our assessment on the possible impact of the CH latitudinal position in modeling their areas. In addition, the sample covers the extended maximum, declining, and early minimum phases of Solar Cycle 24, from 2012 to 2017, enabling the investigation of potential solar activity effects in reconstructing CHs and thus in the choice of the source surface height, an idea that has been suggested before (Arden et al., 2014; Lee et al., 2011).

Out of the 15 CHs, 11 are latitudinally and 3 longitudinally elongated, while one is rather small and bears a more round appearance. Regarding their CoM latitude, 5 and 3 CHs are low latitude ones positioned in the Northern and Southern Hemispheres, respectively, while 5 and 2 CHs are midlatitude ones in Northern and Southern Hemispheres accordingly. Due to known weaknesses on magnetic field and EUV observations in polar regions (i.e., line-of-site effects), no polar CHs were selected for this study; however, the CH on the 3 January 2017 is clearly connected to a polar CH and is an exception to our sample. In this particular case we do consider the polar part that is visible in the EUV image, acknowledging the impact this will have on the result. The CH on 20 December 2016 appears to be associated to a polar one as well. A faint channeling between the CH and the polar one is visible in the EUV images. Nevertheless, we assess it individually, as its boundaries can be defined and are separated from those of the polar CH. The sample also consists of CHs exhibiting different level of patchiness that is defined by the presence within the CH of large areas with a dipole magnetic field configuration (i.e., 3 January 2017) or due to the CH consisting of a cluster of small dark regions (i.e., 27 March 2013).

2.3. Extracting CH Boundaries With CATCH

The CH boundaries were extracted using CATCH (Heinemann et al., 2019), an intensity threshold algorithm that is modulated by the intensity gradient along the CHs boundary. The SSW-IDL-written GUI enables the user to optimize the threshold used for the CH extraction by considering the average intensity profile at the

boundary to find the highest gradient. CATCH operates under the basic assumption that the optimal boundary lies where the intensity gradient is strongest. Additionally, CATCH is the first algorithm that estimates the uncertainties in the extraction to quantify the boundary. Generally, CATCH can be used to detect and extract CHs from multiple spacecrafts (SDO, SOHO, and STEREO), but for this study we used only the EUV 193 Å filtergrams from AIA/SDO. For better quantifying the uncertainties in the PFSS+SCS computed open magnetic field when comparing to the coronal remote sensing observations, in addition to the optimal CH boundary (as defined by CATCH), we also define lower and upper bounds for each CH. The lower and upper bounds present a significantly overestimated and underestimated threshold for the extraction. For further information on the algorithm, we refer to Heinemann et al. (2019). Line-of-sight effects can introduce errors in the boundary extraction of the CH with CATCH; however, these errors are of the order of 2 to 8 arcseconds. EUHFORIA modeling domain is divided in a mesh grid that has resolution of 2° per pixel. Thus, the errors introduced by CATCH in the boundary location is below the EUHFORIA output resolution.

2.4. Reconstructing CH Areas With EUHFORIA

The reconstruction of open flux areas was done using EUHFORIA. For each of the selected CHs we run the coronal model of EUHFORIA for a large sample of $[R_i, R_{ss}]$ heights. To define the height pairs, we started with R_i taking the value of $1.3R_\odot$ up to $2.8R_\odot$ with a step of $0.1R_\odot$, and for each R_i we varied R_{ss} from $1.4R_\odot$ to $3.2R_\odot$ with the same step, and the condition that $R_i < R_{ss}$. ADAPT magnetograms, at date-time same as that of the EUV images analyzed, were used as input to EUHFORIA, which then produced maps of the open and closed magnetic regions for the specified input heights R_i and R_{ss}.

To create these open-closed flux maps, the solar surface is divided in a regular mesh consisting of pixels covering $2° \times 2°$ per pixel. For each pixel the procedure assigns a field line and traces it from the solar surface upwards toward the source surface. If the tracked field line is curved below the source surface and can be traced back down to the solar surface, it is assigned as a closed one. Per contra, if the traced field line pierces through the source surface, it is accredited as an open one. Examples of open-closed field areas are given in Figure 3, where dark blue and red colors represent areas of open flux, with positive and negative polarity, respectively, while light blue and orange areas are correspondingly closed flux areas. The light green contours are the optimal CH boundaries derived from EUV observations using CATCH, as described in the previous section. The results presented in this figure are the output of the model run for the default pair of heights, $[2.3, 2.6]R_\odot$. To better visualize the modeled CH area and the overplotted EUV-based boundaries, especially in the cases of very small CHs, we only plot in Figure 3 the front side of the Sun (Earth view). In addition, for CHs that do not extend to polar regions, high latitudes of Northern and Southern Hemispheres are excluded from the images.

3. Results

3.1. CH Reconstruction Using the Default Model Boundary Heights

The examples in Figure 3 display maps based on the default pairs of heights $[2.3, 2.6]R_\odot$ used as default values in EUHFORIA. These values are the ones concluded in McGregor et al. (2008). It is clear from this figure that, for the majority of the CHs, the model runs based on the default heights $[2.3, 2.6]R_\odot$ fail in reconstructing well the area and geometry as compared to the EUV extraction. Not only are the CHs modeled thinner and overall smaller but also for some cases (i.e., 9 June 2012, 23 May 2013, and 18 January 2014) the CHs appear to be shifted. For the CH of 24 June 2014 the model is unsuccessful in modeling open flux both within the expected boundaries and in the surrounding area. This CH seems to be invisible for the PFSS+SCS models in the adopted WSA model. A CH that appears to be well modeled by EUHFORIA is the one on 3 January 2017, which is a southern polar CH with a large extension that reaches to low Northern Hemisphere latitudes. It is worth pointing out, however, that the CH boundaries extracted with CATCH are only for the part of the CH that is visible from Earth's line of sight. This explains why also in the EUHFORIA output open/closed field map we do not focus on longitudes beyond ±90°.

In order to quantify how successful the model is in reconstructing CH areas, we define the coverage parameter, *cov*, which is given by

$$cov = \frac{N_{open}}{N_{total}} * 100[\%], \tag{1}$$

where N_{open} is the number of open flux pixels contained within the optimal CATCH boundaries (green contour) and N_{total} is the total number of pixels enclosed by that same boundary (open and closed flux pixels).
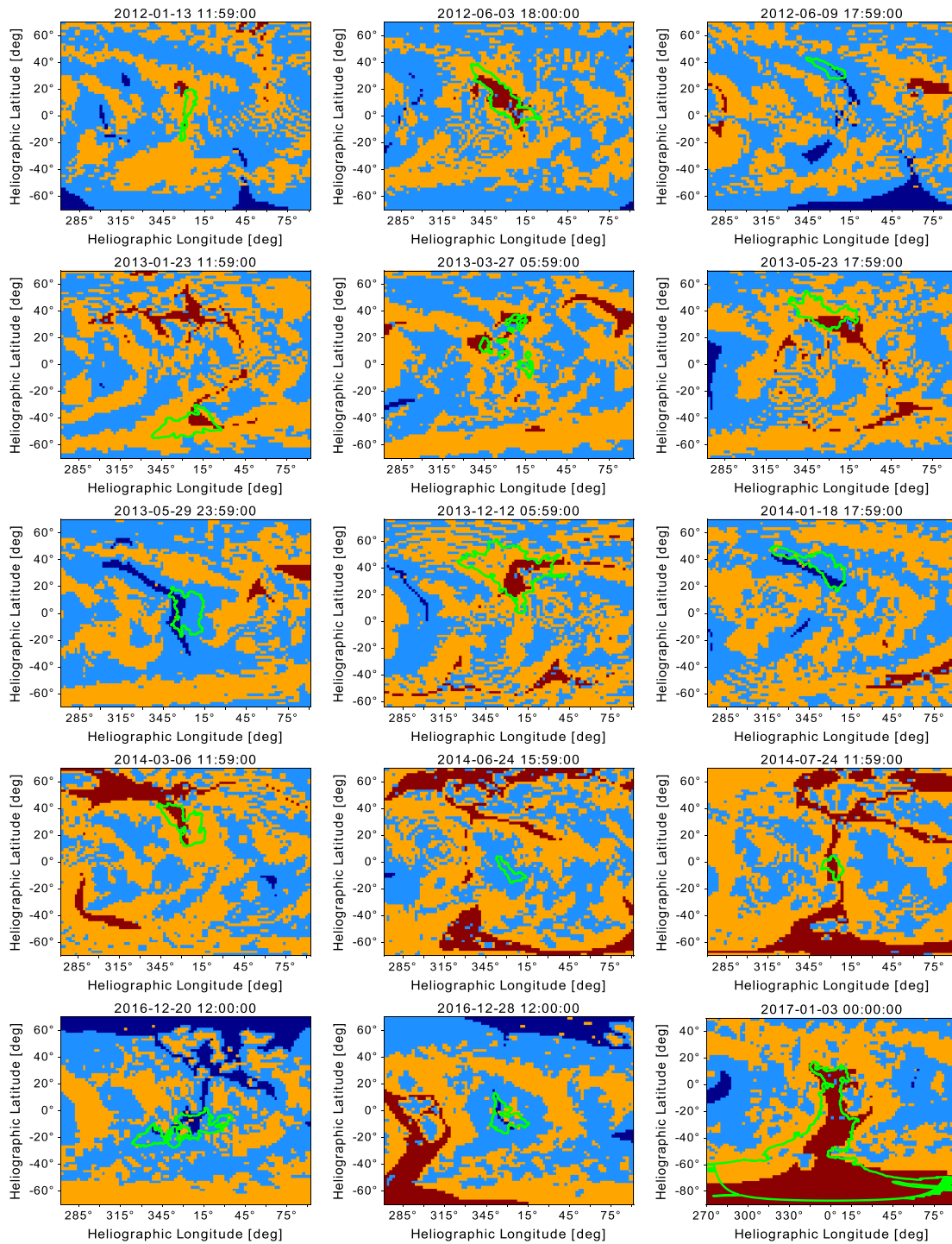
Figure 3. Model generated maps of open-closed field regions based on magnetic field reconstructions by the adopted WSA model in EUHFORIA. Dark blue and red regions represent open field areas of positive and negative polarity, respectively, while cyan and orange are accordingly positive and negative closed field areas. The green outlines overplotted on the maps are the EUV defined optimal boundaries of the CHs as extracted with CATCH. Although the model generates the map for the entire solar surface, we plotted here a fraction of the map aiming to improve the clarity of the CH areas and the overplotted boundaries. Both the CH boundaries extracted with CATCH and the EUHFORIA output are in HEEQ Stonyhurst coordinate system.
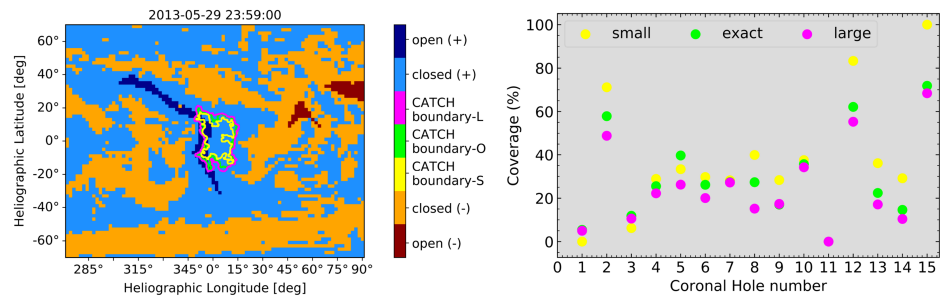
Figure 4. The left panel is an example (CH No7) of how the different boundaries extracted with CATCH can differ from each other. The color scheme for open-closed flux of positive and negative polarity is similar to that in Figure 3. With green color we illustrate the optimal CH boundary extracted with CATCH, while magenta and yellow colored boundaries represent the ones obtained using an underestimated and overestimated thresholds, as described in section 2.3. The right panel shows the coverage, *cov*, achieved by the model when run for the default pair of heights, [2.3, 2.6]$R_\odot$, and when the three different boundaries (optimal, smaller, and larger) are considered for the analysis. The face colors of the circles represent the color of the boundary based on which the calculations were carried out.

Thus, the coverage is the percentage of the expected open field area, enclosed by the green outline in Figure 3, which the model has successfully predicted as open field area. Low coverage indicates not only that the area size of the CH is not correctly modeled but also that the CH could possibly be modeled shifted in space. High coverage suggests that both area size and location are possibly well captured by the model reconstruction of the CH. The coverage for the model results using the default source surface and SCS inner boundary heights, [2.3, 2.6]$R_\odot$, is given in the right panel of Figure 4 as green colored circles. The x axis is the nominal number of the CHs when they are accounted in chronological order (Column 1 of table 1). It can be seen that for 13 out of the 15 CHs we studied, the model gives a coverage below 60%, with the majority of CHs ranking below 30% coverage. This is a clear indication that the model under the default setup does not properly model the CH areas.

We also investigated the possibility of comparing the modeled CH areas to the ones defined by the smaller and larger area boundaries obtained from the EUV images using CATCH. An example of how these boundaries differ from each other is shown in the left panel of Figure 4. In yellow we show the smaller area boundaries and in magenta the larger area boundaries. For most CHs the differences between the areas

Table 1
CH Characteristics Based on Remote Sensing Observations and CATCH Extractions, Where CoM is Center of Mass, Calculated From the Central Meridian Viewed From Earth in Stonyhurst Coordinates and DN Is Data Number (Absolute Counts)

| No	Date-time [UTC]	CoM latitude [°]	CoM longitude [°]	Area [$10^{10}km^2$]	Mean intensity [DN]
1	20120113T12:00	5.01	10.07	2.34 ± 0.12	36.31 ± 0.86
2	20120603T18:00	13.04	0.91	9.69 ± 0.33	31.29± 0.62
3	20120609T18:00	34.97	0.18	2.02 ± 0.16	44.60 ±1.36
4	20130123T12:00	−44.45	4.70	6.03 ± 0.16	27.79 ± 0.62
5	20130327T06:00	16.71	4.93	3.37 ± 0.42	38.28 ± 1.02
6	20130523T18:00	38.61	3.18	6.91 ± 0.36	29.30 ± 0.81
7	20130530T06:01	1.69	2.76	8.07 ± 0.24	26.68 ± 0.56
8	20131212T05:59	36.52	3.75	17.16 ± 0.88	38.59 ± 1.17
9	20140118T17:58	34.53	6.24	6.34 ± 0.34	35.83 ± 1.17
10	20140306T12:00	27.46	3.23	6.71 ± 0.43	38.80 ± 1.09
11	20140624T18:00	−6.74	1.10	1.95 ± 0.06	29.45 ± 0.57
12	20140724T12:10	−3.53	2.21	2.16 ± 0.05	25.70 ± 0.46
13	20161220T12:10	−13.86	0.92	10.55 ± 0.46	22.31 ± 0.54
14	20161228T12:00	−4.77	1.12	4.84 ± 0.16	25.58 ± 0.45
15	20170103T00:00	−43.35	6.21	42.18 ± 0.71	19.00 ± 0.32
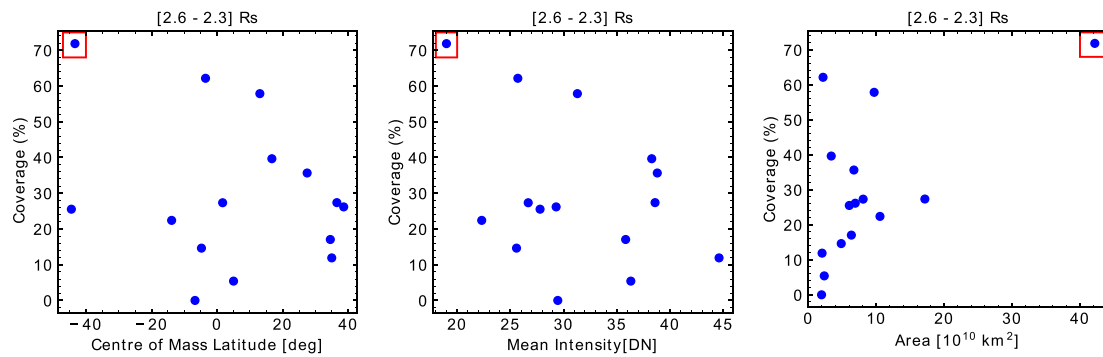
Figure 5. Scatter plots showing the impact on the coverage, *cov*, that the CH characteristics such as the center of mass latitude, the mean intensity, and the CH area have (left, middle, and right panel, respectively). The presented results are based on running the model for the default pair of heights $[2.3, 2.6]R_\odot$ and indicate that neither CoM latitude, mean intensity, or area had any effect in the performance of the model results. The red box encircles the south polar CH with the long extension to equatorial latitudes.

defined by the three different boundaries (small, optimal, and large) is not that substantial. The coverage estimated for these is shown in corresponding colors in the right panel of the same figure. Although smaller area boundaries, as expected, improve the coverage percentage for the majority of the CHs, for some this improvement is not significant (i.e., 23 January 2013, 23 May 2013, 6 March 2014, and 24 June 2014). For three CHs (i.e., 13 January 2012, 9 June 2012, and 27 March 2013), the coverage worsens with the smaller boundaries. An explanation to this is that open flux pixels are lying outside the smaller area boundaries. This concludes that there is no systematic improvement if smaller area boundaries were to be obtained from the EUV observations when a smaller threshold is considered. In a similar manner, larger area boundaries do not worsen the result for all CHs.

3.2. CH Characteristics and Their Effect

The open-closed flux maps given in Figure 3 and the coverage, *cov*, shown in Figure 4 indicate that the model performs better for some CHs comparing to others when the model runs are setup using the default pair of heights. In order to exclude the possibility of the model showing preference in better modeling CHs bearing particular features, we assess how the coverage relates to CH characteristics. The elongation, latitudinal position of CoM, patchiness, area size, and mean intensity are apparent features of a CH that are of interest to this study.

The elongation of a CH can have an effect to the modeled results due to the way the selected magnetograms are constructed. Even though dynamical processes are applied to them, synchronic ADAPT magnetograms best represent the magnetic field on the Sun along the central meridian as viewed from Earth. This suggests that CHs, which are latitudinally elongated and lie within the central meridional zone, can be possibly better modeled when selecting a magnetogram from the date the CH was located there. Thus, a longitudinally elongated CH might not be as accurately modeled at its full length. So when studying a CH on a particular moment, it can also have an impact to the modeled output based on that perspective.

CH mean intensity and area are parameters extracted using CATCH, as described in the section 2.3. The mean intensity is automatically computed with CATCH based on the threshold used for extracting the CH boundaries. It is expected that active regions in the vicinity of a CH will have an impact on its configuration, which is also imprinted on magnetograms, and thus has the potential to affect the modeled CH areas. The sample's average mean intensity is 31.3 DN, and only 6 out of the 15 CHs studied have mean intensity above that value. The size of a CH is expected to affect the width/duration of a high-speed stream as well as its speed and open flux and thus is a parameter we investigate (Hofmeister et al., 2018; Nolte et al., 1976; Rotter et al., 2012; Vršnak et al., 2007). In terms of the area the CH sample consists of both small and large CHs, with the biggest on 3 January 2017 extending from polar to solar equatorial latitudes. The sample mean is 8.7×10^{10} km^2, and four CHs have area above this value.

In Figure 5, the left panel presents the coverage, *cov*, with respect to the CoM latitude. From the level of scatter in the points, it is clear that the latitudinal position of the CH does not affect the performance of the modeled result. The same applies for the other two parameters shown in the middle panel (mean intensity) and the right most panel (area). We know that in estimating the mean intensity of CHs, we have to be
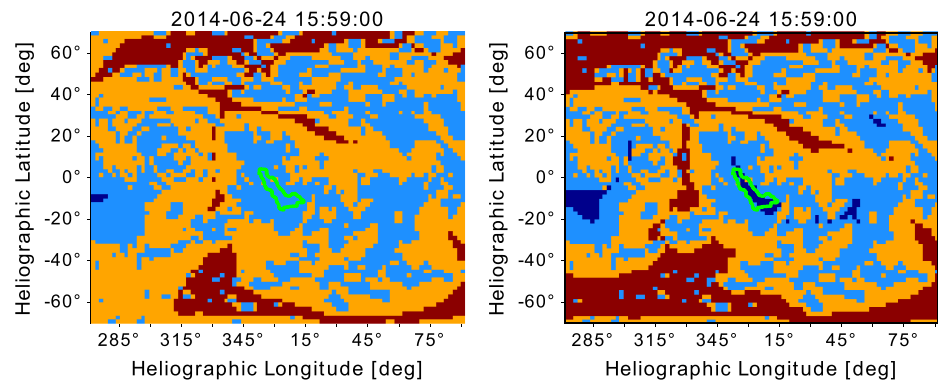
Figure 6. Maps of open-closed flux generated for the same CH by two different model runs. The one on the left resulted by EUHFORIA running for the default pair of heights $[2.3, 2.6]R_\odot$, while the one on the right for the pair $[1.3, 1.8]R_\odot$. It is clear that the CH is not present in the model result on the left but is present and well captured by the run setup based on lower heights. This example highlights the impact the heights of the source surface and the inner boundary of the SCS model have in the modeling result.

aware of multiple factors that influence the uncertainty of the absolute values of the measured intensity. Any instrument (in this case AIA) suffers inevitable depletions (e.g., decreasing sensitivity, aging filters, and others), distortion of optical system, and scattered light to name just a few. But in the context of this study, especially regarding the CH detection, we do not believe that these uncertainties introduce significant errors, as each CH was manually tuned to account for such instrumental and observational changes (see for more details Heinemann et al., 2019). For the case of large CHs we have only one point so the relation between coverage and area remains inconclusive. We also checked whether the visual characteristics of elongation and patchiness of a CH have any effect. No such conclusion could be made; however, the number of CHs is too low for the result to be compelling. We also accounted for the possibility of a coupling of different parameters, for example, area or intensity and CoM latitude, which could have an effect in the modeled results. But even for this scenario no trend is apparent with respect to the coverage. One conclusion that could be made is that all CHs located in the Southern Hemisphere of the Sun have low mean intensity, while those in the northern have high. This can possibly be a solar cycle related effect, since we studied CHs from one SC only (SC24), and indeed, from 2013 to 2015 Southern Hemisphere clearly dominated both in the number and in the area size of sunspots (Li et al., 2019; see also sunspot number information at http://www.sidc.be/silso/ssngraphics). Our sample size is rather small for an unambiguous conclusion to be made, so a more detailed analysis of a larger CH sample is necessary.

3.3. Assessing for Systematic Shifting and Solar Cycle Trends

Maps of open-closed flux indicated the possibility of shifting of the modeled CH areas with respect to the expected location. To assess this, we investigated the likelihood of a systematic shifting. All directions (eastward/westward and northward/southward) were investigated. In addition, we considered both a 2° and a 4° shifts in each direction. From this analysis no systematic effect could be identified. The role of CH characteristics, such as mean intensity, elongation, size, CoM latitude, and hemispheric position, in shifting effects was evaluated independently. Regardless of whether the sample is assessed as a whole or divided in groups based on the CH characteristics, the conclusion for possible shifting remained negative for all cases.

In earlier studies (Arden et al., 2014; Lee et al., 2011; Levine, 1982) the concept of a solar cycle-dependent source surface height has been suggested, that is, varying within the course of the solar cycle, as well as from one solar cycle to another. We investigated this prospect at first for the whole CH sample and then by separating CHs to groups based on their apparent characteristics mentioned also in the shifting investigation. We found no solar cycle trends when assessing the result for the default heights, but also for our full set of $[R_i, R_{ss}]$ heights discussed below. We note that the number of considered CHs is rather small and, therefore, no conclusive results can be drawn about the systematic shift. In addition, the period over which the sample extends does not cover a complete solar cycle, so to understand solar cycle effects on the modeling output, it is important for such a study to consider a sample that spans over the entire solar cycle.
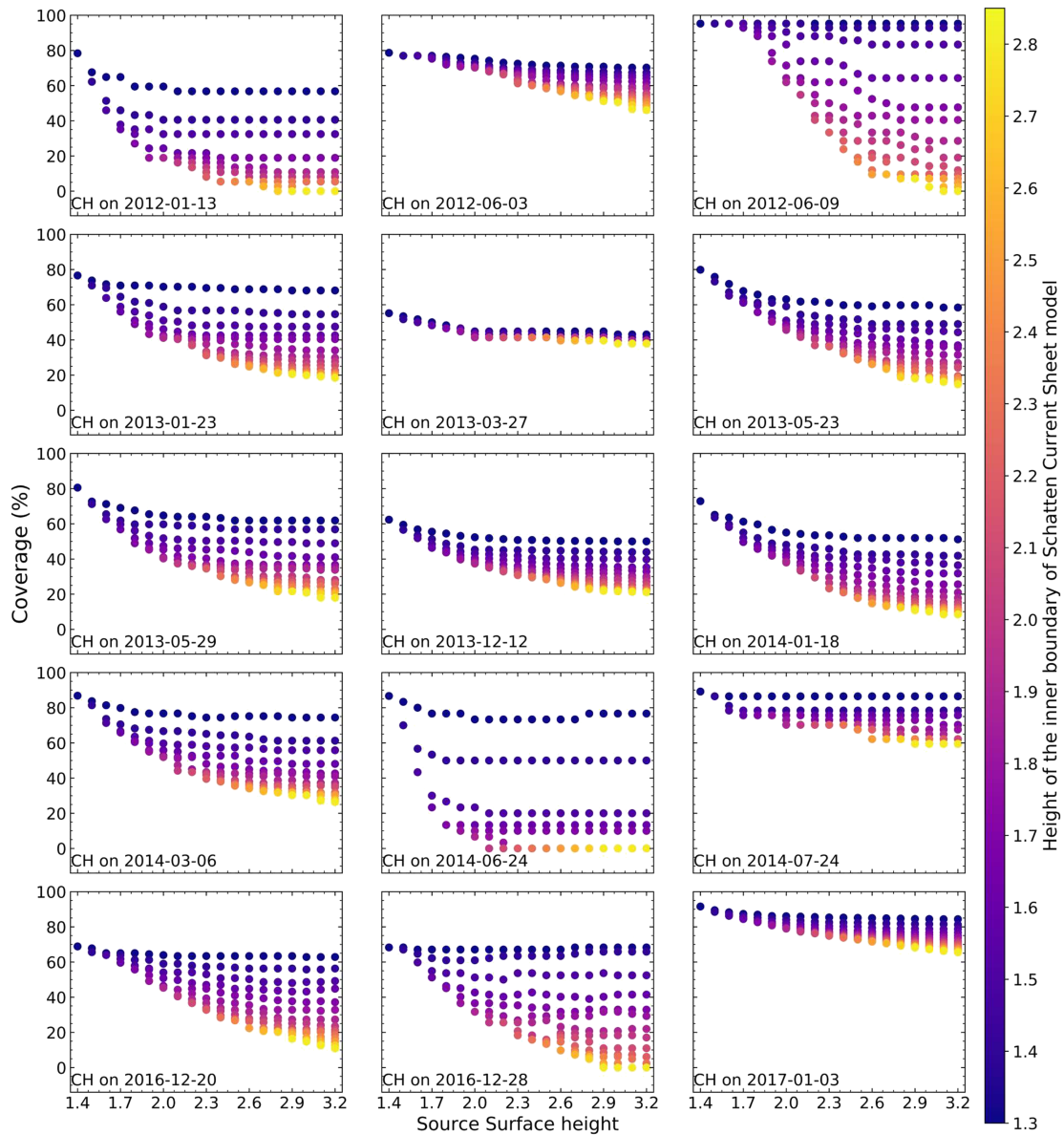
Figure 7. Collective results of model runs based on all the 184 pairs of heights for the source surface and the inner boundary of the SCS model. Each panel presents the results for one CH, and they are placed in chronological order. The *x* axis is the source surface height, and the color bar is the height of the inner boundary of the SCS model increasing from dark to bright colors. The *y* axis shows the coverage, *cov*. As can be seen, for the majority of CHs best coverage is achieved for lower height values for the inner boundary of the SCS model.

3.4. Finding the Optimum Paired Values for [R_i, R_{ss}]

After running the model for all 184 pairs of [R_i, R_{ss}] heights, it was made evident that lowering the source surface height significantly improved the modeled CHs. One very clear example is that of 24 June 2014, shown in Figure 6. This particular CH was invisible in the open-closed flux maps created with the boundaries placed at the default pair of heights. As can be seen from the right panel in Figure 6, the model nicely maps the CH area when a lower pair of heights is considered. We specifically compare the default heights output to this one because the source surface height of $1.8R_\odot$ has been suggested by other studies as a better choice for particular periods and has been used in earlier studies for comparison purposes (e.g., Lee et al., 2011).

Figure 7 is a collective plot for the coverage resulting from the model runs for each of the 184 height pairs and the 15 CHs. Each panel represents the results for a particular CH, while the *x* axis is the source surface height; the *y* axis the coverage, *cov*; and the color map the height of the inner boundary of the SCS model, R_i. The striking feature in this figure is that for the vast majority of the CHs reducing R_i significantly improves
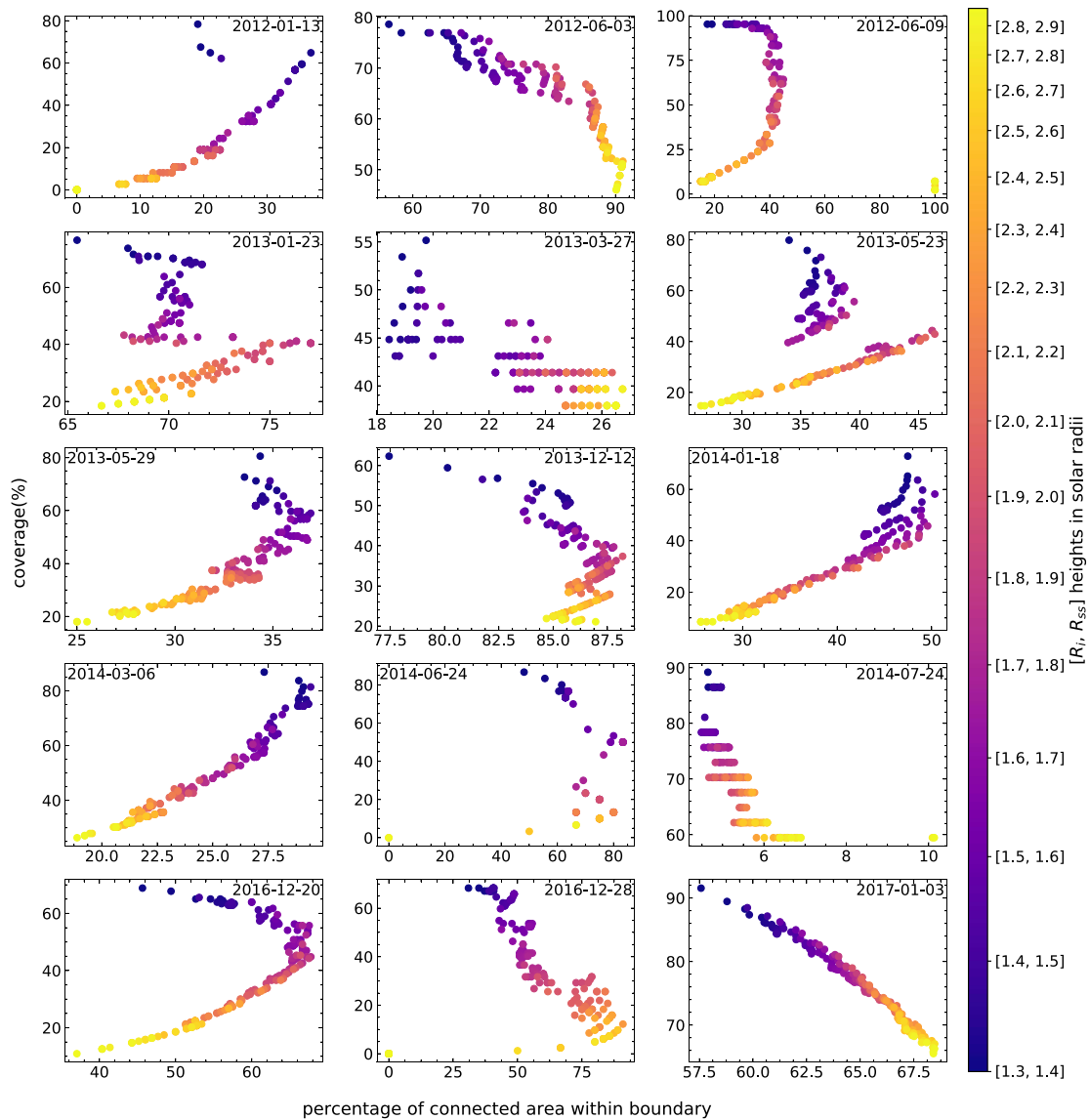
Figure 8. Each panel depicts how, for a particular CH, coverage, *cov*, and CA_{in} change when EUHFORIA runs are set up based on different pair of heights $[R_i, R_{ss}]$. For most CHs a saturation limit is reached beyond which the amount of open flux pixels lying inside the expected from EUV observations area is significantly lower than those lying outside.

the modeled result; that is, the modeled open flux areas grow to cover more of the total expected area outlined by the EUV defined CH boundaries and thus better capture it. This is reflected in the improvement of the coverage, *cov*, parameter plotted on the *y* axis of Figure 7. For some cases the coverage even rises from 0% to almost 100%. Overall, a lower source surface height has the same effect; however, for a fixed low value R_i a decrease in the source surface height does not necessarily have a high impact. The large CH that consisted of the southern polar one and its long extension to equatorial latitudes was very well modeled by EUHFORIA run with the default values. Lowering the values of the pair of heights below the default ones did result in improvement of the coverage; however, as it was already high the improvement was not significant (within 10%). The CH on 27 March 2013 is a very patchy CH that is not well modeled by EUHFORIA's adaptation of the WSA. The coverage is below 60% regardless of the selected pair of heights considered for running EUHFORIA. Another patchy CH, but significantly less patchy than that on 27 March 2013, is the CH on 20 December 2016. This CH is a bit better modeled when lower values of the pair of heights are considered, but the coverage remained below 70%. Reconstruction of these strongly (27 March 2013) and moderately (20 December 2016) patchy CHs suggests that the model might have difficulty in reconstructing patchy CHs. It
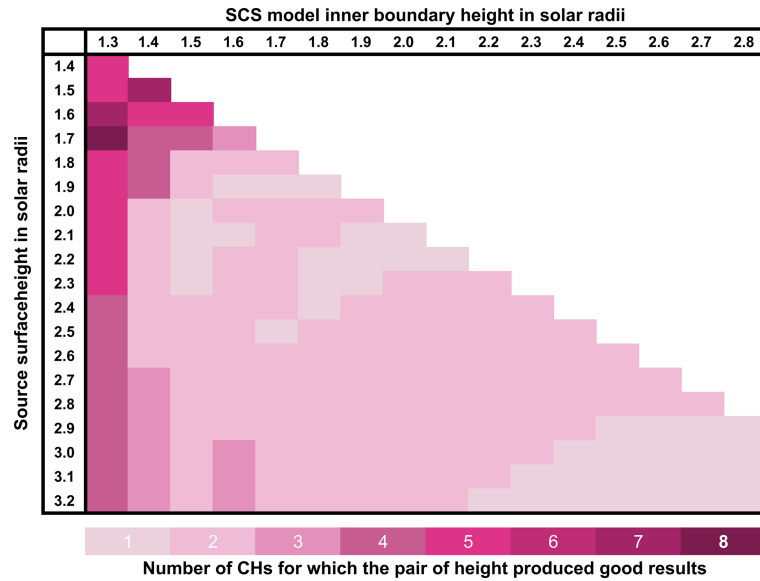
Figure 9. Collective table of all 184 pair of heights for which the model was tested. The color in each shell indicates that this pair of heights produced good results both in *cov* and CA_{in} for a certain number of CHs, as indicated in the color map. The most successful pairs of heights, that is, the ones that were successful for more CHs, are collected on the top left corner of the table where lower height values can be found.

will be interesting for this to be investigated further by considering a larger sample of patchy CHs. Also, it will be interesting to assess possible impact in modeling high-speed streams originating from these CHs.

Even though there is a clear indication that a pair of lower heights will result in a significantly improved coverage for all CHs, not a single pair could be specified as the ideal one. In addition, lowering the two heights results in opening more flux to the heliosphere, not only within the CH areas but also outside; namely, open field areas appear to be overestimated. This is illustrated in Figure 6 where the modeled CH area extends beyond the EUV-defined boundaries, green outline, both to the north and to the south. This total open field area, appearing in blue color on the map, we call the connected pixels area. The portion of this connected area that lies outside the EUV-defined CH boundary we call connected pixels outside, while the portion that lies within the CH boundary we call connected pixels inside. This feature is present in all CH cases and rises the question of how low one can place the two heights, $[R_i, R_{ss}]$, in order to best model the CH area, but without overestimating the open flux outside the EUV defined CH boundaries. To answer that question, we consider the connected pixels area. To identify these areas, we apply the region growth method by selecting seed pixels within the CH area that are assigned as open field. We calculated the total number of connected open flux pixels, N_{total}, and divided them to those that lie within the boundaries, N_{in}, and those that lie outside, N_{out}. From these we define the percentage of connected area within the boundary, CA_{in}, which is given by

$$CA_{in} = \frac{N_{in}}{N_{total}} * 100[\%]. \qquad (2)$$

In Figure 8 we plot this parameter against the coverage. We can see that for the majority of the CHs both parameters at first increase but then the system reaches a point where the percentage of connected area that lies within the boundaries starts decreasing. This implies that although open flux pixels grow, the majority lies outside the EUV defined boundaries. If flux was opening only inside the boundaries, then the curves would be approximately linear. This does not happen though and a saturation point is reached from which further decreasing of the two heights opens more flux outside the boundaries than inside. Following the standard paradigm that the primary source of open flux are CH areas, we can conclude that too low heights lead to nonphysical results due to cutting actually closed loops. This is an important finding since it limits how low the two heights can be. From the same figure one can notice that for some CHs there is a double saturation limit.

These saturation limits identified in Figure 8 can be used in order to constrain the possible pairs of boundary heights to those that provide an improved result both in coverage, *cov*, and CA_{in}. We define two criteria with

the first being that the coverage parameter needs to be above 60% and the second is that CA_{in} should lay no less than 5% from the saturation limit. Although, for most CHs the coverage is above 70%, for four of them (i.e., 27 March 2013, 12 December 2013, 20 December 2016, and 28 December 2016), the maximum coverage is well below that value, which is the reason for this 60% limit. Especially for the CH on 27 March 2013 the coverage parameter is below 55%; thus, a special limit of minimum 50% coverage is applied. For 8 out of the 15 CHs the value of CA_{in} is below 50%. To this, we include the CH on 9 June 2012 for which the high values of CA_{in} are only for when the coverage is below 10%, which indicates that the number of open flux pixels is extremely low. A $CA_{in} < 50\%$ is the result of having more open flux lying outside the CH area defined by the EUV boundaries for all the model runs performed. For some of the CH, a secondary saturation limit can be identified less than 10% from the first one, which, however, results in better coverage without affecting greatly CA_{in}. For those cases we do consider the second saturation limit for the CA_{in} in investigating the optimal $[R_i, R_{ss}]$ pair. After analyzing the results for each CH, we collected the pairs of heights that justify the criteria posed. The table is presented in Figure 9. The color map indicate the number of CHs for which the pair fitted the criteria. Although all the height pairs fulfill the criteria for at least one CH, some appear as good candidates more frequently. As can be seen in the table low heights of the SCS model inner boundary (below $1.5R_\odot$) are better options for successfully reconstructing CH areas ($cov > 60\%$), while the selection of the source surface height varies more strongly. Although for the CH sample studied here these heights gave better results in terms of the coverage, it is important to highlight that there still can be open flux growth outside the expected from observations CH areas. So the use of the heights need to be done with caution.

4. Conclusion and Discussion

As already discussed in other works (e.g., Arden et al., 2014; Linker et al., 2017; Wallace et al., 2019), discrepancies exist between in situ measured at 1 AU and model computed open flux using the PFSS model, and subsequently the WSA model. Considering the standard paradigm that CHs are primary sources of open flux (Linker et al., 2017; Mackay & Yeates, 2012), testing whether CHs are properly modeled is a logical step. Linker et al. (2017) highlighted the importance for the model output to match CHs observed in EUV emission. They used automatically detected CHs to quantitatively make comparisons between the PFSS model output and CHs areas. Earlier, Lowder et al. (2014) thoroughly computed open flux based on automatically detected CHs and compared the result to the PFSS estimations. For the period Linker et al. (2017) investigated, placing the source surface height at $2.5R_\odot$ resulted in significantly underestimated open field area and flux. They also concluded that lowering the source surface, although improved the open flux value, it overestimates the areas of open flux.

In this work we presented a collective study assessing the capability of the PFSS+SCS part of the adopted WSA model by EUHFORIA forecasting tool in modeling CH areas. Although values between 1.6 to 3.25 solar radii are considered allowed for the source surface height, a commonly used value is $2.5R_\odot$ (e.g., Arge & Pizzo, 2000; Riley et al., 2015; Wallace et al., 2019). On the other hand, McGregor et al. (2008) concluded that for the modified WSA model that they presented, and which is also adopted in EUHFORIA, the optimal heights of the source surface and the SCS model inner boundary are $[2.3, 2.6]R_\odot$, which we considered as the default pair of heights. Other studies suggested an even lower or higher source surface height (Lee et al., 2011; Phillips et al., 1994) or even a solar cycle varying source surface (Arden et al., 2014; Levine, 1982). We considered 184 pairs of heights aiming to investigate whether the modeled result can be improved. We selected 15 CHs having CoM latitude within the central meridional zone of the Sun, and a variety of morphology defined by their elongation, area size, intensity, and level of compactness. Using EUHFORIA, we reconstructed the CH area based on model runs for the 184 pairs. The modeled areas were compared to those derived with CATCH using EUV imaging observations.

Our main result is that the default heights employed so far, $[2.3, 2.6]R_\odot$, fail to model the expected CH areas and/or their locations, with coverage below 60%. This suggests that CH areas are not properly modeled using the default setup. This might provide some explanation for the discrepancy between the open flux output by the WSA model and that measured in situ at Earth (Linker et al., 2017; Riley et al., 2015; Wallace et al., 2019). In some cases even the whole CH was missed. Our analysis clearly shows that lower heights (R_i below $1.5R_\odot$ and R_{ss} below $2.3R_\odot$) lead to an improved coverage ($cov > 60\%$) of the CH areas defined by the EUV extracted boundaries. In other words, the modeled open field area better represents the EUV observed CH area. However, it also strongly results in opening flux outside the EUV defined CH boundaries as well. More precisely, modeled open flux areas mark a much larger region than the EUV defined CH areas. This

suggests the possibility that open flux can originate beyond CHs, which diverge from the standard paradigm according which CHs are the sources of open field. This result also suggests that EUV-defined CHs might only provide a lower limit of the actual open field region. This last point is in agreement with Linker et al. (2017) result, that is, that lowering the heights leads to overestimating open flux regions. Assuming that the standard paradigm for open flux origin is correct, this raises the question of how low the source surface height can be placed in order to properly model CH areas and at the same time not model excess open flux areas outside the EUV defined boundaries. Considering modeling the SW speed at 1 AU, it will be very interesting to see the effect of the modeled open flux areas outside the EUV defined boundaries can have. Our analysis also shows that it is rather the height of the inner boundary of the SCS model and not of the source surface that has a stronger effect on the modeled result. We also deduced that low values of this boundary lead to better results in terms of CH area reconstruction. It is noteworthy that this result is based on analyzing a CH sample from only one solar cycle and considers CHs located in the central meridional zone. Increasing the size of the sample and also extending it over a larger period of time can potentially lead to different height selection.

Although following different techniques Lowder et al. (2014), Linker et al. (2017), and Wallace et al. (2019) overplotted automatically detected CHs on synoptic magnetic maps but still resulted in underestimated open flux, according to Linker et al. (2017), the result could only be improved by considering areas larger than the detected CHs, leading them to the conclusion that either synoptic maps underestimate the solar magnetic flux or that CHs are not the sole source of open flux. In addition, there are studies that challenge the certainty that the open flux from in situ measurements should be an exact match to that modelled close to the Sun, arguing that there might be other processes/factors affecting it, as suggested, for example, in Lockwood et al. (2009), where they found that the excess open flux between models and in situ measurements can be explained by kinematic effects of variations of the SW speed. Thus, opening the question of whether one to one comparison is a sensible approach.

Arden et al. (2014), Levine (1982), and Lee et al. (2011) investigated the possibility of a solar cycle varying source surface height and concluded that a lower source surface height during solar minimum periods is required. We investigated this possibility, but we identified no solar cycle trends in the success of the model in reconstructing CH areas; however, capturing the whole cycle could improve the results. In addition, we investigated a possible latitude dependence; however, the latitudinal position of the CH did not have any effect on the modeled results. These are interesting results, which, however, need to be considered with care due to rather small sample size. A more detailed analysis, considering a larger number of CHs, spanning over more than one solar cycle and over all solar cycle phases, and having more variety in their latitudinal positions, can potentially lead to a different outcome.

An interesting remark is that for the CH on 24 July 2014 a channeling to a polar CH was present regardless of the selected pair of heights. This was also appearing for other CHs in the sample when lower heights were selected for the source surface and the inner boundary of the SCS model. The idea of CHs being linked to polar ones via narrow passages in the photosphere has been discussed in, for example, Antiochos et al. (2007, 2011). It will be interesting to investigate this aspect on a larger sample of CHs.

At this point it is worth pointing out that, although comparing model reconstructed open field areas to EUV extracted CH areas is a concept already incorporated in other studies (e.g., Lowder et al., 2014; Linker et al., 2017), the two do not necessarily capture the same phenomena. We assume that a CH, and subsequently an open flux area, can be well identified in EUV images as a dark region. However, the areas surrounding CHs might also contain open field, even though due to strong presence of closed field there they appear bright in EUV images and are thus not recognized as part of the CHs (Linker et al., 2017). As it has been suggested, open flux could also originate from outside CHs (Fisk & Zurbuchen, 2006), such as foot points of active regions, which do not appear dark in emissions (Linker et al., 2017; Luhmann et al., 2008, and references therein). Therefore, due to these obscuration effects, the EUV images provide an open flux area that can be an underestimate of the actual one. Moreover, magnetograms are momentary representations of the magnetic field configuration of the photosphere and thus do not capture the short-scale dynamic processes that can contribute to the total open field areas. This can lead to underestimated modeled open flux areas. The effect of a nontime-evolving input boundary has also been suggested in Riley et al. (2019), where they are comparing MHD and PFSS reconstruction of the structure of the coronal magnetic field using the same input magnetogram. Although Riley et al. (2019) reduced the source surface height to $2.0R_\odot$

for the PFSS model, still, the predicted open flux areas were smaller than the MHD prediction, which has been considered in the past as more definitive. The impact of time-dependent phenomena that are obscured in EUV, of the rapid evolution of the photospheric field, of the steady state assumption of the PFSS model and of the synoptic maps considered should not be neglected (Luhmann et al., 2002, 2008, 2013; Wallace et al., 2019).

It is necessary to mention that the outcome of this study, and other similar studies before it, is focused on how the two free parameters involved in the PFSS+SCS, and subsequently in the WSA model, can affect the modeled results. Saying that we aim to bring forward that the missing open flux in the model outputs might likewise require fine tuning of the other free parameters involved in the model, an idea also discussed in Wallace et al. (2019). EUHFORIA currently implements an expansion of spherical harmonics method to analytically solve the Laplace equation of WSA model. However, that method can give rise to two effects in the modeling output (Tran, 2009; Tóth et al., 2011). The first one is a ring-like pattern present in low latitudes, that can be visible in the open-closed field maps in Figure 3. This pattern is due to strong isolated pixels associated to active regions. Therefore, if an active region is close to a CH, it can generate the ring-like pattern that can affect the shape of the modeled open field area. The second effect is a ring-like patterns near the poles similar to Gibbs phenomenon in the Fourier analysis. The choice of the number of spherical harmonics used in the model is important, since using higher spherical harmonics can reduce the first effect but enhances the second. Thus, it is necessary to work in improving the model to reduce the ring patterns. Future work should also focus on improving the statistics and also on different aspects of the model outcomes, that is, CH areas, open flux at Earth, velocity of high-speed streams, and current sheet position.

References

Altschuler, M. D., & Newkirk, G. (1969). Magnetic fields and the structure of the solar corona. I: Methods of calculating coronal fields. *Solar Physics*, *9*, 131–149. https://doi.org/10.1007/BF00145734

Antiochos, S. K., DeVore, C. R., Karpen, J. T., & Mikić, Z. (2007). Structure and dynamics of the Sun's open magnetic field. *The Astrophysical Journal*, *671*(1), 936–946. https://doi.org/10.1086/522489

Antiochos, S. K., Mikić, Z, Titov, V. S., Lionello, R., & Linker, J. A. (2011). A model for the sources of the slow solar wind. *The Astrophysical Journal*, *731*(2), 112. https://doi.org/10.1088/0004-637X/731/2/112

Arden, W. M., Norton, A. A., & Sun, X. (2014). A "breathing" source surface for Cycles 23 and 24. *Journal of Geophysical Research: Space Physics*, *119*, 1476–1485. https://doi.org/10.1002/2013JA019464

Arge, C. N., Henney, C. J., Koller, J., Compeau, C. R., Young, S., MacKenzie, D., & Harvey, J. W. (2010). Air Force Data Assimilative Photospheric Flux Transport (ADAPT) model. In *Twelfth International Solar Wind Conference* (pp. 343–346). https://doi.org/10.1063/1.3395870

Arge, C. N., Hildner, E., Pizzo, V. J., & Harvey, J. W. (2002). Two solar cycles of nonincreasing magnetic flux. *Journal of Geophysical Research*, *107*(A10), 1319. https://doi.org/10.1029/2001JA000503

Arge, C. N., & Pizzo, V. J. (2000). Improvement in the prediction of solar wind conditions using near-real time solar magnetic field updates. *Journal of Geophysical Research*, *105*, 10,465–10,480. https://doi.org/10.1029/1999JA000262

Fisk, L. A., & Zurbuchen, T. H. (2006). Distribution and properties of open magnetic flux outside of coronal holes. *Journal of Geophysical Research*, *111*, A09115. https://doi.org/10.1029/2005JA011575

Gressl, C., Veronig, A. M., Temmer, M., Odstrčil, D., Linker, J. A., Mikić, Z., & Riley, P. (2014). Comparative study of MHD modeling of the background solar wind. *Solar Physics*, *289*(5), 1783. https://doi.org/10.1007/s11207-013-0421-6

Heinemann, S. G., Temmer, M., Heinemann, N., Dissauer, K., Samara, E., Jerčić, V., et al. (2019). Statistical analysis and catalog of non-polar coronal holes covering the SDO-Era using CATCH. *Solar Physics*, *294*, 144. https://doi.org/10.1007/s11207-019-1539-y

Hickmann, K. S., Godinez, H. C., Henney, C. J., & Arge, C. N. (2015). Data assimilation in the ADAPT photospheric flux transport model. *Solar Physics*, *290*, 1105–1118. https://doi.org/10.1007/s11207-015-0666-3

Hinterreiter, J., Magdalenic, J., Temmer, M., Verbeke, C., Jeberaj, I. C., Samara, E., et al. (2019). Testing the background solar wind modelled by EUHFORIA. arXiv e-prints, arXiv:1907.07461. https://doi.org/10.1007/s11207-019-1558-8

Hoeksema, J. T., & Scherrer, P. H. (1986). An atlas of photospheric magnetic field observations and computed coronal magnetic fields: 1976–1985. *Solar Physics*, *105*, 205–211. https://doi.org/10.1007/BF00156388

Hoeksema, J. T., Wilcox, J. M., & Scherrer, P. H. (1982). Structure of the heliospheric current sheet in the early portion of sunspot cycle 21. *Journal of Geophysical Research*, *87*, 10,331–10,338. https://doi.org/10.1029/JA087iA12p10331

Hoeksema, J. T., Wilcox, J. M., & Scherrer, P. H. (1983). The structure of the heliospheric current sheet—1978–1982. *Journal of Geophysical Research*, *88*, 9910–9918. https://doi.org/10.1029/JA088iA12p09910

Hofmeister, S. J., Veronig, A., Temmer, M., Vennerstrom, S., Heber, B., & Vršnak, B. (2018). The dependence of the peak velocity of high-speed solar wind streams as measured in the ecliptic by ACE and the STEREO satellites on the area and co-latitude of their solar source coronal holes. *Journal of Geophysical Research: Space Physics*, *123*, 1738–1753. https://doi.org/10.1002/2017JA024586

Jian, L. K., Russell, C. T., Luhmann, J. G., MacNeice, P. J., Odstrcil, D., Riley, P., et al. (2011). Comparison of observations at ACE and Ulysses with Enlil model results: Stream interaction regions during Carrington Rotations 2016–2018. *Solar Physics*, *273*(1), 179. https://doi.org/10.1007/s11207-011-9858-7

Lee, C. O., Luhmann, J. G., Hoeksema, J. T., Sun, X., Arge, C. N., & de Pater, I. (2011). Coronal field opens at lower height during the Solar Cycles 22 and 23 minimum periods: IMF comparison suggests the source surface should be lowered. *Solar Physics*, *269*, 367–388. https://doi.org/10.1007/s11207-010-9699-9

Lee, C. O., Luhmann, J. G., Odstrcil, D., MacNeice, P. J., de Pater, I., Riley, P., & Arge, C. N. (2009). The solar wind at 1 AU during the declining phase of Solar Cycle 23: Comparison of 3D numerical model results with observations. *Solar Physics*, *254*(1), 155–183. https://doi.org/10.1007/s11207-008-9280-y

Lemen, J. R., Title, A. M., Akin, D. J., Boerner, P. F., Chou, C., Drake, J. F., & Waltham, N. (2012). The Atmospheric Imaging Assembly (AIA) on the Solar Dynamics Observatory (SDO). *Solar Physics*, *275*, 17–40. https://doi.org/10.1007/s11207-011-9776-8

Levine, R. H. (1982). Open magnetic fields and the solar cycle—Part One—Photospheric sources of open magnetic flux. *Solar Physics*, *79*(2), 203–230. https://doi.org/10.1007/BF00146241

Levine, R. H., Altschuler, M. D., & Harvey, J. W. (1977). Solar sources of the interplanetary magnetic field and solar wind. *Journal of Geophysical Research*, *82*, 1061–1065. https://doi.org/10.1029/JA082i007p01061

Levine, R. H., Schulz, M., & Frazier, E. N. (1982). Simulation of the magnetic structure of the inner heliosphere by means of a non-spherical source surface. *Solar Physics*, *77*(1-2), 363–392. https://doi.org/10.1007/BF00156118

Li, F. Y., Xiang, N. B., Xie, J. L., & Xu, J. C. (2019). The present special Solar Cycle 24: Casting a shadow over periodicity of the North-South Hemispherical asymmetry. *The Astrophysical Journal*, *873*(2), 121. https://doi.org/10.3847/1538-4357/ab06bf

Linker, J. A., Caplan, R. M., Downs, C., Riley, P., Mikic, Z., Lionello, R., et al. (2017). The open flux problem. *The Astrophysical Journal*, *848*, 70. https://doi.org/10.3847/1538-4357/aa8a70

Lockwood, M., Owens, M., & Rouillard, A. P. (2009). Excess open solar magnetic flux from satellite data: 2. A survey of kinematic effects. *Journal of Geophysical Research*, *114*, A11104. https://doi.org/10.1029/2009JA014450

Lowder, C., Qiu, J., Leamon, R., & Liu, Y. (2014). Measurements of EUV coronal holes and open magnetic flux. *The Astrophysical Journal*, *783*(2). https://doi.org/10.1088/0004-637X/783/2/142

Luhmann, J. G., Lee, C. O., Li, Y., Arge, C. N., Galvin, A. B., Simunac, K., et al. (2009). Solar wind sources in the late declining phase of Cycle 23: Effects of the weak solar polar field on high speed streams. *Solar Physics*, *256*(1-2), 285–305. https://doi.org/10.1007/s11207-009-9354-5

Luhmann, J. G., Li, Y., Arge, C. N., Gazis, P. R., & Ulrich, R. (2002). Solar cycle changes in coronal holes and space weather cycles. *Journal of Geophysical Research*, *107*(A8), 1154. https://doi.org/10.1029/2001JA007550.

Luhmann, J. G., Li, Y., Riley, P., Arge, C. N., Liu, Y., & Detoma, G. (2008). Challenges created by active regions in global models for space weather uses. *Subsurface and Atmospheric Influences on Solar Activity*, *383*, 133.

Luhmann, J. G., Petrie, G., & Riley, P. (2013). Solar origins of solar wind properties during the Cycle 23 solar minimum and rising phase of cycle 24. *Journal of Advanced Research*, *4*(3), 221–228. https://doi.org/10.1016/j.jare.2012.08.008

Mackay, D. H., & Yeates, A. R. (2012). The Sun's global photospheric and coronal magnetic fields: Observations and models. *Living Reviews in Solar Physics*, *9*(1), 6. https://doi.org/10.12942/lrsp-2012-6

MacNeice, P., Jian, L. K., Antiochos, S. K., Arge, C. N., Bussy-Virat, C. D., DeRosa, M. L., et al. (2018). Assessing the quality of models of the ambient solar wind. *Space Weather*, *16*, 1644–1667. https://doi.org/10.1029/2018SW002040

McGregor, S. L., Hughes, W. J., Arge, C. N., & Owens, M. J. (2008). Analysis of the magnetic field discontinuity at the potential field source surface and Schatten Current Sheet interface in the Wang-Sheeley-Arge model. *Journal of Geophysical Research*, *113*, A08112. https://doi.org/10.1029/2007JA012330

Nolte, J. T., Krieger, A. S., Timothy, A. F., Gold, R. E., Roelof, E. C., Vaiana, G., et al. (1976). Coronal holes as sources of solar wind. *Solar Physics*, *46*(2), 303. https://doi.org/10.1007/BF00149859

Owens, M. J., Spence, H. E., McGregor, S., Hughes, W. J., Quinn, J. M., Arge, C. N., et al. (2008). Metrics for solar wind prediction models: Comparison of empirical, hybrid, and physics-based schemes with 8 years of L1 observations. *Space Weather*, *6*, S08001. https://doi.org/10.1029/2007SW000380

Pesnell, W. D., Thompson, B. J., & Chamberlin, P. C. (2012). The Solar Dynamics Observatory (SDO). *Solar Physics*, *275*(1-2), 3–15. https://doi.org/10.1007/s11207-011-9841-3

Phillips, J. L., Balogh, A., Bame, S. J., Goldstein, B. E., Gosling, J. T., Hoeksema, J. T., et al. (1994). Ulysses at 50° south: Constant immersion in the high-speed solar wind. *Geophysical Research Letters*, *21*(12), 1105–1108. https://doi.org/10.1029/94GL01065

Pomoell, J., & Poedts, S. (2018). EUHFORIA: European heliospheric forecasting information asset. *Journal of Space Weather and Space Climate*, *8*, A35. https://doi.org/10.1051/swsc/2018020

Riley, P., Ben-Nun, M., Linker, J. A., Mikic, Z., Svalgaard, L., Harvey, J., et al. (2014). A multi-observatory inter-comparison of line-of-sight synoptic solar magnetograms. *Solar Physics*, *289*(3), 769–792. https://doi.org/10.1007/s11207-013-0353-1

Riley, P., Downs, C., Linker, J. A., Mikic, Z., Lionello, R., & Caplan, R. M. (2019). Predicting the structure of the solar corona and inner heliosphere during Parker Solar Probe's first perihelion pass. *The Astrophysical Journal*, *874*(2), L15. https://doi.org/10.3847/2041-8213/ab0ec3

Riley, P., Linker, J. A., & Arge, C. N. (2015). On the role played by magnetic expansion factor in the prediction of solar wind speed. *Space Weather*, *13*, 154–169. https://doi.org/10.1002/2014SW001144

Riley, P., Linker, J. A., Mikić, Z., Lionello, R., Ledvina, S. A., & Luhmann, J. G. (2006). A Comparison between Global Solar Magneto-hydrodynamic and Potential Field Source Surface Model Results. *The Astrophysical Journal*, *653*, 1510–1516. https://doi.org/10.1086/508565

Rotter, T., Veronig, A. M., Temmer, M., & Vršnak, B. (2012). Relation between coronal hole areas on the Sun and the solar wind parameters at 1 AU. *Solar Physics*, *281*(2), 793–813. https://doi.org/10.1007/s11207-012-0101-y

Schatten, K. H. (1971). Current sheet magnetic model for the solar corona. *Cosmic Electrodynamics*, *2*, 232–245.

Schatten, K. H., Wilcox, J. M., & Ness, N. F. (1969). A model of interplanetary and coronal magnetic fields. *Solar Physics*, *6*, 442–455. https://doi.org/10.1007/BF00146478

Schulz, M. (1997). Non-spherical source-surface model of the heliosphere: A scalar formulation. *Annales Geophysicae*, *15*, 1379–1387. https://doi.org/10.1007/s00585-997

Schulz, M. (2008). Non-spherical source-surface model of the corona and heliosphere for a quadrupolar main field of the Sun. *AGU Spring Meeting Abstracts*, *44*, SH44A–04.

Schulz, M., Frazier, E. N., & Boucher, D. J. (1978). Coronal magnetic-field model with non-spherical source surface. *Solar Physics*, *60*(1), 83. https://doi.org/10.1007/BF00152334

Schwenn, R. (2006a). Solar wind sources and their variations over the solar cycle. *Space Science Reviews*, *124*(1-4), 51–76. https://doi.org/10.1007/s11214-006-9099-5

Schwenn, R. (2006b). Space weather: The solar perspective. *Living Reviews in Solar Physics*, *3*(1), 2. https://doi.org/10.12942/lrsp-2006-2

Tóth, G., van der Holst, B., & Huang, Z. (2011). Obtaining potential field solutions with spherical harmonics and finite differences. *The Astrophysical Journal*, *732*(2), 102. https://doi.org/10.1088/0004-637X/732/2/102

Tran, T. (2009). Improving the predictions of solar wind speed and interplanetary magnetic field at the Earth (Ph.D. Thesis), California: University of California, Los Angeles.

Vršnak, B., Temmer, M., & Veronig, A. M. (2007). Coronal holes and solar wind high-speed streams: I. Forecasting the solar wind parameters. *Solar Physics*, *240*(2), 315–330. https://doi.org/10.1007/s11207-007-0285-8

Wallace, S., Arge, C. N., Pattichis, M., Hock-Mysliwiec, R. A., & Henney, C. J. (2019). Estimating total open heliospheric magnetic flux. *Solar Physics*, *294*, 19. https://doi.org/10.1007/s11207-019-1402-1

Wang, Y.-M. (2009). Coronal holes and open magnetic flux. *Space Science Reviews*, *144*(1-4), 383–399. https://doi.org/10.1007/s11214-008-9434-0

Wang, Y.-M., Hawley, S. H., & Sheeley, N. R. Jr. (1996). The magnetic nature of coronal holes. *Science*, *271*, 464–469. https://doi.org/10.1126/science.271.5248.464

Wang, Y.-M., & Sheeley, N. R. Jr. (1990). Solar wind speed and coronal flux-tube expansion. *The Astrophysical Journal*, *355*. https://doi.org/10.1086/168805

Wang, Y.-M., & Sheeley, N. R. Jr. (1992). On potential field models of the solar corona. *The Astrophysical Journal*, *392*, 310–319. https://doi.org/10.1086/171430

Wang, Y.-M., & Sheeley, N. R. Jr. (1995). Solar implications of ULYSSES interplanetary field measurements. *The Astrophysical Journal Letters*, *447*, L143. https://doi.org/10.1086/309578

Wang, Y.-M., & Sheeley, N. R. Jr. (2003). On the topological evolution of the coronal magnetic field during the solar cycle. *The Astrophysical Journal*, *599*, 1404–1417. https://doi.org/10.1086/379348